Effect of slide burnishing on corrosion potential in ASTM A-36 steel

A. Saldaña-Robles[a], M. Zapata-Torres[b], J. Moreno-Palmerin[c], and A. Márquez-Herrera[a,*]

[a]*Departamento de Ingeniería Agrícola, División de Ciencias de la Vida,*
Campus Irapuato-Salamanca, Universidad de Guanajuato, Irapuato, Guanajuato 36500, México.
*e-mail: amarquez@ugto.mx
[b]*Instituto Politécnico Nacional, CICATA Unidad Legaria, Ciudad de México, 11500, México.*
[c]*Departamento de Minas, Metalurgía y Geología, División de Ingenierías,*
Campus Guanajuato, Universidad de Guanajuato, Irapuato, Guanajuato 36500, México.

This study investigates the corrosion potential of ASTM A-36 steel after slide burnishing using different applied forces. Milled samples of ASTM A-36 steel were subjected to slide burnishing surface treatment. The burnishing process was carried out with forces of 150 N, 300 N, and 450 N, at a travel speed of 100 mm/min. The effects of burnishing on the phase and chemical composition of the material were analyzed using Grazing Incidence X-ray Diffraction and X-ray photoelectron spectroscopy, which indicated no changes in the crystalline phase or chemical composition of the material. Corrosion potential measurements were performed using the Tafel test. The results showed that as the burnishing force increased, the corrosion potential shifted to lower values. Additionally, roughness analysis suggested that the change in corrosion potential was attributed to plastic deformation caused by the burnishing process. The increased mechanical work exerted on the material during burnishing may be the underlying reason for the observed shift towards lower corrosion potentials with higher applied forces.

1. Introduction

There are multiple techniques used for surface finishing of metallic materials, primarily applied to machinery parts. Processes such as electrochemical finishing, burnishing, electropolishing, abrasive flow machining, shot peening, etc. [1-5] can be employed to improve surface finish. Slide burnishing provides several benefits as improving surface hardness, roughness and dimensional accuracy of a workpiece. These is achieved by generating compressive residual stresses on both the surface and subsurface of the workpiece [6].

Toloei *et al.* [7] states that as surface roughness decreases, the corrosion potential (E_{corr}) shifts towards the noble direction. Additionally, Abosrra *et al.* [8] shows that the corrosion potential of 316L stainless steel is dependent on chloride concentration and surface roughness. As chloride concentration and roughness increase, the corrosion potential becomes less noble. While some authors have studied the effect of burnishing on corrosion, including roughness, grain size, etc. [9-14], and these studies clearly indicate a change in the corrosion potential, this aspect is not or partially addressed in their results and discussions. Consequently, many authors attribute the alteration in corrosion potential mainly to roughness. Therefore, the objective of this study is to investigate the effect of roughness resulting from turning on the corrosion potential of ASTM A-36 steel, as a first step. In a second step, evaluate the influence of the plastic deformation caused by slide burnishing on the corrosion potential of previously milling surfaces. Understanding the change in corrosion potential is significant because it depends on variations in both the anodic and cathodic reactions. For instance, if the cathodic reaction remains constant, a decrease in corrosion potential can be attributed to an increase in the anodic reaction, indicating that the metal becomes more active. Conversely, an increase in corrosion potential can be attributed to a decrease in the anodic reaction, suggesting that the metal becomes more noble. A positive shift in the corrosion potential signifies that anodic corrosion is primarily retarded [15, 16].

2. Experimental

An ASTM A-36 steel with 25 mm in diameter and about 5 mm long was used as substrate. Table I indicates the chemical composition of this steel.

TABLE I. Chemical composition of the ASTM A-36 steel rod (in % wt).

C	Mn	P	S	Si	Ni	Cr	Mo	Cu	Ti	V	Sn
0.14	0.86	0.016	0.026	0.220	0.14	0.17	0.04	0.28	0.001	0.044	0.009

In a first step, samples of ASTM A-36 steel rod were turned using a conventional lathe, to evaluate the influence of the roughness surface on the corrosion potential. The cutting conditions used on surface samples were a speed of 460 rpm, depth of cut of 0.1016 mm, dry condition and four feed rates 0.0356 mm/rev (14M), 0.0711 mm/rev (28M), 0.1194 mm/rev (47M) and 0.1422 mm/rev (56M).

In a second step, to study the effect of the slide burnishing force on the corrosion potential of ASTM A-36 steel, four samples were milled using a Fadal VMC 3016 CNC Vertical Machining Center. The samples were milling in a CNC machine instead of tuned in the conventional lathe, due the CNC machine reduces the standard deviation of the roughness compared with a conventional lathe for the same sample [17], this to minimize the influence of initial roughness in the samples and improve the evaluation just of the effect of the burnishing force. One of the four samples was not treated (control), the other three were burnished in an area of 15×15 mm using a diamond slide burnishing tool. The parameters were burnishing force of 150 N (B-150N), 300 N (B-300N) and 450 N (B-450N), travel speed of 100 mm/min following a step-cross toolpath with a 50 % step over distance of the spherical tip trace, 0.29 mm, which was obtained by experimental tests for these specific burnishing forces. X-ray diffractograms were recorded by using Grazing Incidence X-ray Diffraction (GIXRD) at 1°. X-ray photoelectron spectroscopy (XPS) was used to analyze the chemical environment structures of iron. The XPS analysis was performed using a K alpha model from Thermo Scientific. Both general and high-resolution spectra were obtained from the samples. To calibrate the obtained spectra, the binding energy of the C 1s line at 284.5 eV was chosen as the reference peak. The Fe signal curves were fitted by using the XPSpeak41 software. The corrosion evaluation was conducted by Tafel (potentiodynamic polarization) technique. An Ag/AgCl (3 M KCl) electrode and a carbon disc were used as reference and

counter electrode, respectively. An area of 1 cm^2 of steel substrate was used as the working electrode. The reference electrode was verified in a typical Daniell cell, where high purity copper and zinc electrodes were immersed in a solution of copper (II) sulfate and zinc sulfate (from Sigma-Aldrich), respectively. The copper and zinc electrodes were verified by -the Bragg Bentano method- X-ray Diffraction (XRD) from 20° to 80° with a step of 0.02°2s, and a scanning electron microscope (SEM) Jeol JSM-5300 equipped with Kelvex energy dispersive spectrometer (EDS) model delta 1. Before the measurements, an open circuit potential (OCP) was computed for 3600 s. Tafel tests were carried-out a ± 150 mV scan relative E_{corr} at a 0.5 mV/s potential speed. Then, Tafel curves were fitted to find both corrosion current (I_{corr}) and E_{corr} by using the VersaStudio corrosion test software which performs a numerical fit to Tafel equations. The cross-plane thermal conductivity of samples was measured by a home-made thermal analyzer. Amplitude roughness indicators as arithmetic average deviation of the roughness profile (R_a), average maximum height of the roughness profile (R_z) and maximum height of the roughness profile (R_t) were determined using a roughness meter Mitutoyo® surf test SJ-310 according to the ISO 4287 standard. For every sample, five measurements of each roughness indicator were recorded using a cut-off length of 0.8 mm, evaluation length of 4.8 mm and measure speed of 0.5 mm/s.

3. Results and discussions

Figure 1 shows the X-ray diffractograms of the Cu and Zn electrodes used to verify the quality of the Ag/AgCl (3 M KCl) reference electrode. The positions of the diffraction peaks associated with the cubic and hexagonal crystal structure of Cu and Zn, obtained respectively from JDPDS cards 040836 and 040831 from the Powder Diffraction Files 2 (PDF-2) Database, are also shown.
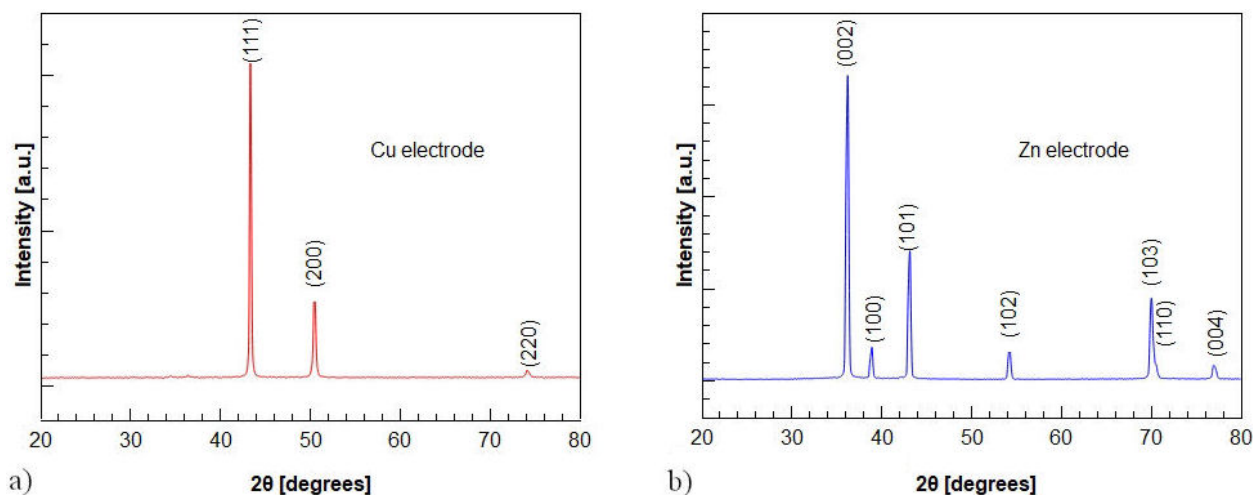

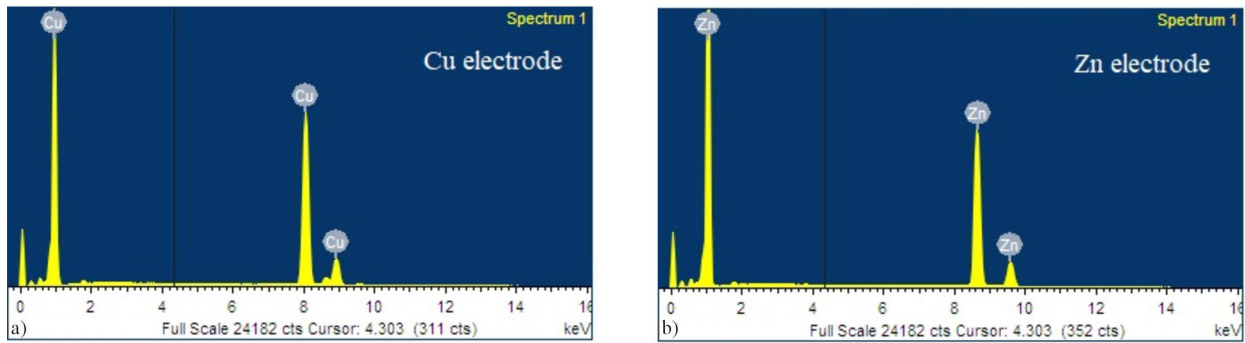FIGURE 1. X-ray diffraction patterns of Cu and Zn electrode.

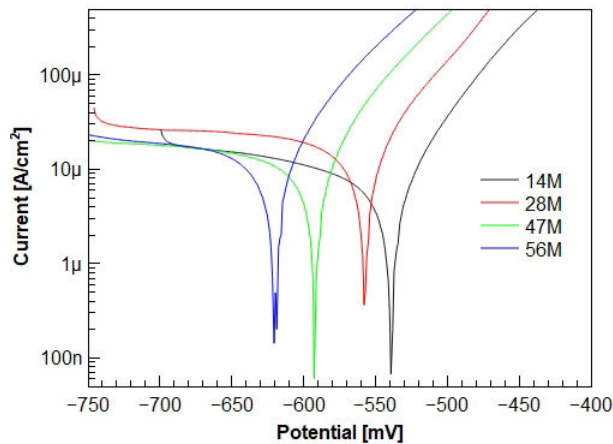FIGURE 2. EDS measurements of Cu and Zn electrode.

FIGURE 3. Polarization Tafel plots for turned samples in NaCl 3.5 %wt.

FIGURE 4. X-ray diffraction patterns of milled (control) and burnished (B-150N) sample.

The atomic composition was also evaluated by EDS in the same set of Cu and Zn electrodes. Figure 2 shows the EDS profiles of pure copper and zinc, respectively. Also, a typical noise peak is shown at very low energies. Hence, according to the X-ray diffractograms and EDS measurements, the electrodes are composed of Cu and Zn.

Figure 3 shows Tafel spectra obtained during the testing of turned samples in NaCl aqueous solution.

It is known that the main threats to surface integrity come from the plastic deformation of the workpiece during the machining process, and the plastic deformation could change if we modify any turning parameter, such as feed rate [18, 19]. In this sense, Fig. 3 shows that corrosion potential shifts to the left while more feed rate is used in lathe. Table II shows the change in corrosion potential due the plastic deformation caused by the feed rate.

To reduce the standard deviation of the initial roughness on the samples to be burnished, samples were milled (Con-
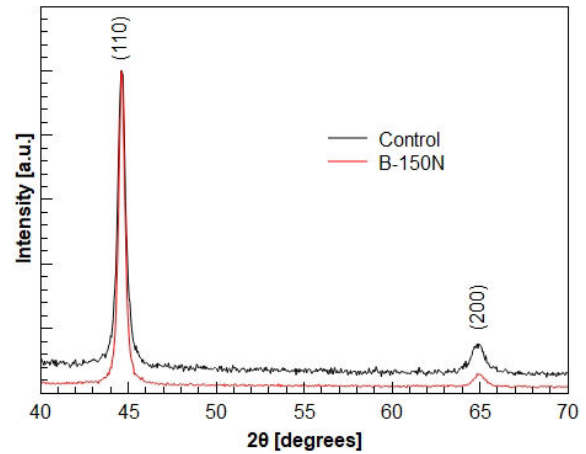

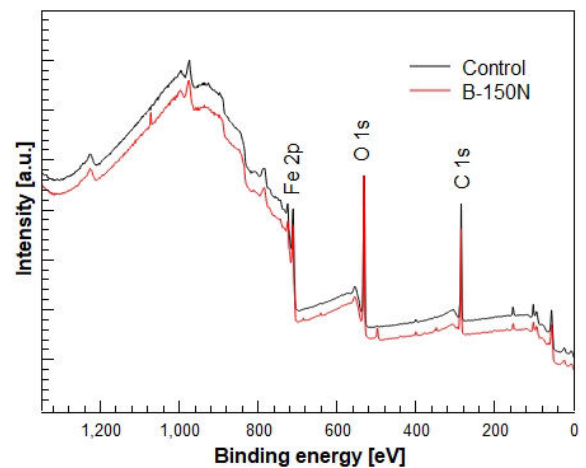
FIGURE 5. X-ray photoelectron spectroscopy (XPS) spectrum for milled (control) and burnished (B-150N) sample.

trol sample) and then burnished using a Fadal VMC 3016 CNC Vertical Machining Center applying a force of 150 N (B-150N), 300 N (B-300N) and 450 N (B-450N). In order to verify that there are no phase changes on the material surface due to the temperatures generated by the friction between the

TABLE II. The values of E_{corr} and I_{corr} for turned samples.

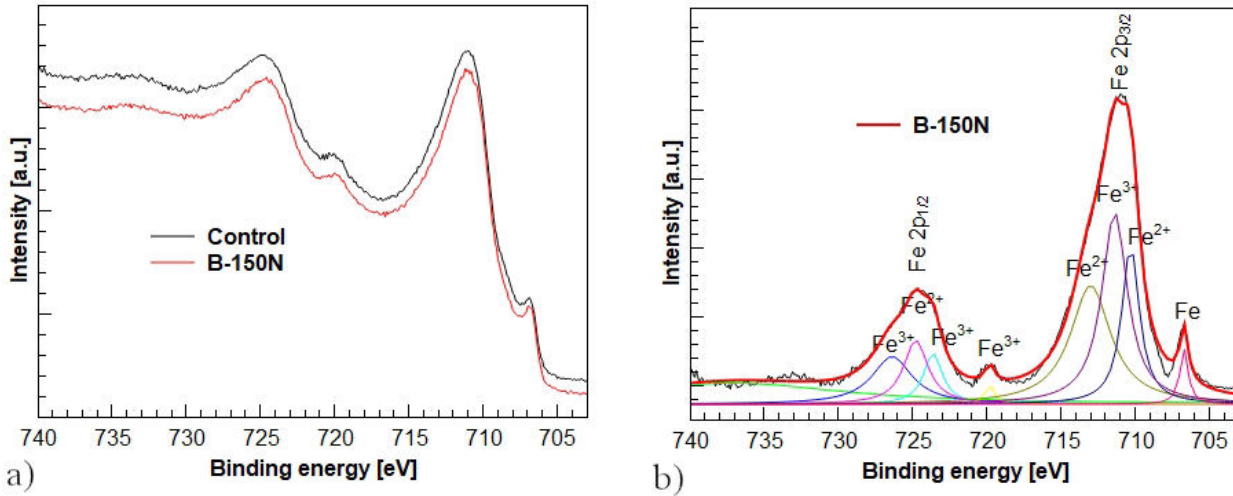| Parameter	14M	28M	47M	56M
E_{corr} (mV)	-539.313	-557.44	-592.16	-620.243
I_{corr} (A/cm^2]	9.823	21.938	17.144	20.612

FIGURE 6. High resolution XPS spectrum associated to the a) Fe binding energies and b) the deconvolution of the Fe signal for sample B-150 N.

burnishing tool and the surface, prior to the corrosion tests, which could alter the results, as an example, Fig. 4 shows GIXRD patterns for unburnished (control) and burnished (B-150N) sample. According to JDPDS card No. 060696 from the PDF-2 Database, the diffraction peak positions confirm only Fe-α phase on unburnished and burnished sample without any other phase, suggesting that milling and burnishing do not induce any other phase on the surface of the material.

Figure 5 shows the insights into the chemical environment of the elements of the sample surface, mainly iron, performed by x-ray photoelectron spectroscopy (XPS). The general survey XPS spectrum show main peaks as Fe, O and C. Clearly the general spectrum are similar on both samples.

Figure 6a) shows the high resolution XPS spectrum associated to the Fe binding energies for the control and the burnished sample with 150 N. Due the spectrum are similar for both samples, Fig. 6b) shows a peak fit analysis of the Fe 2p$_{1/2}$ and Fe 2p$_{3/2}$ signal profiles for B-150N sample. It shows the deconvolution of the signals that are attributed to Fe, Fe^{2+} and Fe^{3+} [20]. The positions of the peaks were obtained from the x-ray photoelectron spectroscopy database of NIST [21]. This result confirms that, derived from the temperature due to the friction between the material surface and the tool during the burnishing process in dry condition, burnishing does not change the chemical composition of the material surface. The presence of iron oxides (Fe^{2+} and Fe^{3+}) are the native oxides presented in all steel.

To analyze the influence of plastic deformation from the perspective of burnished force on samples, and then establishes the corrosion potential based on applied force, Tafel curves are presented in Fig. 7.

Figure 7 shows that burnishing process provides a similar corrosion resistance to all samples, however, the corrosion potential moves to the left while more force is used in burnishing as shown in Table III This could be due to the residual stress induced by burnishing [11]. Furthermore, a shift towards more positive values (to the right) can be observed
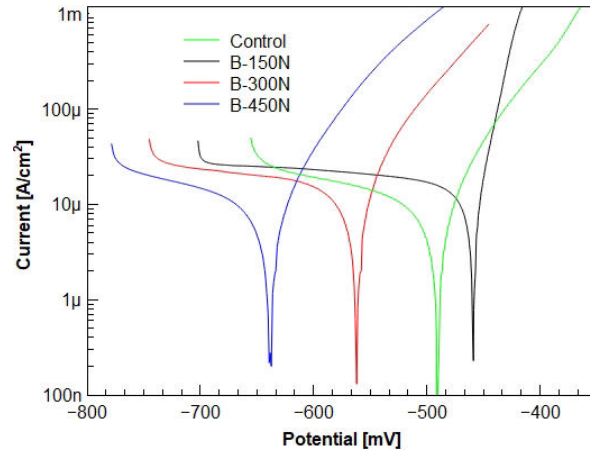

FIGURE 7. Polarization plots for control and burnished samples using a force of 150 N (B-150 N), 300 N (B-300 N) and 450 N (B-450 N) in NaCl 3.5 %wt.

in the corrosion potential of sample B-150N compared to the control sample (non-burnished). This behavior is consistent with what has been reported by Al-Qawabeha *et al.* [13]. It is interesting to note that Figs. 2 and 6 suggest that the turned and burnished surfaces become less noble when increasing cutting speed and burnishing force, respectively, due to the increased level of compressive residual stress. In contrast, Salahshoor *et al.* [22] reported that burnished surfaces become more noble when increasing rolling force; however, they used high forces and did not control the finishing surface before burnishing.

TABLE III. The values of E_{corr} and I_{corr} for burnished samples.

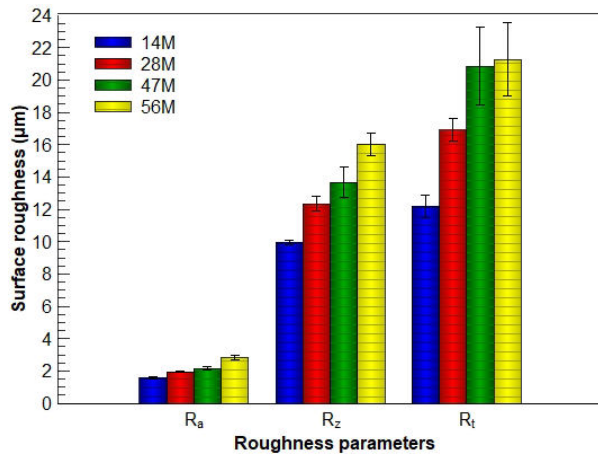| Parameter	Control	B-150N	B-300N	B-450N
E_{corr} (mV)	-490.514	-459.029	-562.092	-638.553
I_{corr} (A/cm^2)	9.531	14.707	21.169	17.544

FIGURE 8. Roughness parameters obtained after turning process at different feeds.

FIGURE 9. Roughness parameters obtained after milling and milling-burnishing processes.

Potential values, shown in Table III, confirm that the corrosion potential shifted to the left while more force is used in burnishing due the residual stress induced by burnishing.

The values of the cross-plane thermal conductivity (89.0 W/m-K) were similar for the control and burnished sample. Maybe because plastic deformation is not sufficient to induce changes in the thermal property of the material.

Figure 8 shows the R_a, R_z and R_t roughness values obtained after conventional turning for 14M, 28M, 47M and 56M samples, respectively. As expected, the results indicate that surface roughness parameters increased due to increasing feed rate, this is because increasing the feed rate leads to a larger separation between consecutive positions of the cutting insert causing a greater distance between peaks and valleys [23, 24]. An increase of the feed rate from 0.0356 mm/rev to 0.1422 mm/rev caused that R_a, R_z and R_t roughness parameters increasing by 44.4%, 37.9% and 42.7%, respectively.

Figure 9 shows the R_a, R_z and R_t roughness values after milling (control) and milling-burnishing specimens (B-150N, B-300N and B-450N). All roughness parameters were reduced with the three burnishing forces applied.
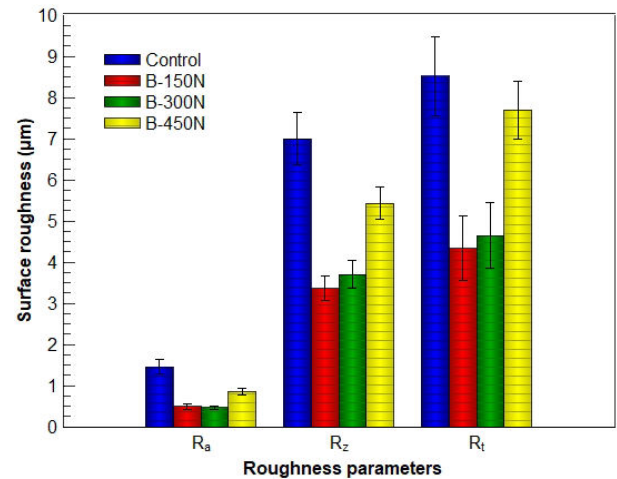
Although in Fig. 9 the roughness values presented a similar value for the burnishing forces of 150 N and 300 N, Fig. 10 illustrates that the burnishing force of 300 N causes enough high surface plastic deformation to produce the footprint of the deforming element of the tool on the workpiece surface, while a burnishing force of 150 N produces a smoothing of the initial surface profile without marks. Therefore, the optimal burnishing force for this material using the milling conditions employed in this study is between 150 N and 300 N. For the burnishing force of 450 N, a greater plastic deformation occurs on workpiece surface in comparison with 300 N, causing an increase in R_a, R_z and R_t roughness values. According to the results of Fig. 9 between the control and burnishing specimens, using the burnishing force of 150 N allows reducing R_a, R_z and R_t by 66.2%, 51.9% and 49.1%, respectively.

Figure 8 gives the impression that the change of potential is due to roughness. However, maintaining the same roughness on samples but increasing the burnishing force, even obtaining less roughness, the opposite is presented, as shown
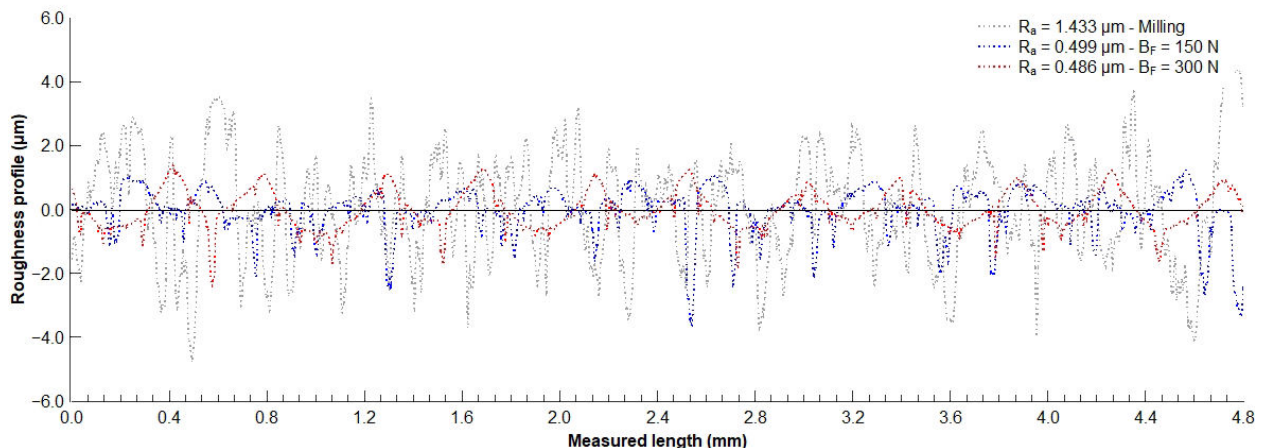

FIGURE 10. Typical roughness profiles after milling and milling-burnishing specimens of ASTM A-36 steel.

in the Figs. 8 and 9, which suggests that corrosion potential shifted is due to the plastic deformation (residual stress) and possibly does not due to the roughness or with a smaller contribution.

In order to explain the residual stress effect on the material, it is known that the first law of thermodynamics establishes that

$$dU = dQ - \delta W. \tag{1}$$

For a stationary thermodynamic system as corrosion, dU denotes the change in internal energy, dQ is the energy exchange across the system boundary as heat, and δW represents the sum of the work exerted by the system onto its surrounding environment. It can be demonstrated [25] that the change in Gibbs' free energy is equal to the maximum amount of work that a system can perform to the surroundings while undergoing a spontaneous change when temperature and pressure are maintained constant, as corrosion:

$$\Delta G = -\delta W. \tag{2}$$

In an electrical or electrochemical process as corrosion, $\delta W = \delta W_e$. δW_e corresponds to an electrical work that can be defined as the product of nFE in which the potential difference between anode and cathode is E, and the total charge transferred during the reaction (nF):, then the electrical work (δW_e) done by the cell must be nFE, where n is the number of moles of electrons and F the Faraday constant. At equilibrium, there is no corrosion and Gibbs' free energy is given by the following equation: $\Delta G = -nFE$. However, when a burnishing is done in material, it induces a compressing residual stress on treated surface by the effect of plastic deformation [11, 26]. In this way, δW should be rewritten as:

$$\delta W = \delta W_e + \delta W_m, \tag{3}$$

where δW_e corresponds to electrical work done to the surroundings and δW_m denotes the mechanical work done to the system from burnishing that produces a change in the Gibbs' free energy, ΔG, which can reduce the activation energy for an atom to leave the metal lattice and get into the solution. The positive sign is the result of the work done from the surrounding to the system that corresponds the work done by increasing its potential energy. In this sense, this amount of mechanical work done could be the reason why the curves shifted to lower potentials with respect to reference electrode while more force is used in burnishing, and this could be interpreted as a crystalline structure change or grain refinement due a residual stress by burnishing [9, 12]. Although some authors attribute the change in the corrosion potential due to the surface finish of the material, such as roughness, this study suggests that the plastic deformation [27] that it might experience should not be neglected. Further investigations can build upon these findings to explore the interplay between burnishing, residual stress, and corrosion behavior.

4. Conclusions

Slide burnishing was performed by using forces of 150 N, 300 N and 450 N. The Tafel results confirm that the corrosion potential is shifted to the left while more force is used in burnishing process, because burnishing induces compresive residual stresses over the surface by the effect of plastic deformation. It denotes a mechanical work done that produces a change in the Gibbs' free energy in the material and it could be the reason that the corrosion potential is shifted.

In conclusion, this study demonstrates that slide burnishing on ASTM A-36 steel with varying applied forces can affect the corrosion potential. The findings suggest that the plastic deformation induced by the burnishing process and the resulting increase in mechanical work contribute to the observed shift in corrosion potential towards lower values with higher burnishing forces. These insights enhance our understanding of the effects of burnishing on the corrosion behavior of ASTM A-36 steel and provide valuable information for optimizing the surface treatment process to mitigate corrosion risks in practical applications.

Acknowledgments

1. P. Pa, Continuous finishing processes using a combination of burnishing and electrochemical finishing on bore surfaces, *Int J Adv Manuf Techno* **49** (2010) 147, https://doi.org/10.1007/s00170-009-2386-z.

2. S. Kumar *et al.*, Effect of processing condition on abrasive flow machining process: A review, *Materials Today: Proceedings* (2023), https://doi.org/10.1016/j.matpr.2022.12.237.

3. J. Maximov *et al.*, Effects of Heat Treatment and Diamond Burnishing on Fatigue Behaviour and Corrosion Resistance of AISI 304 Austenitic Stainless Steel, *Applied Sciences* 13 (2023), https://doi.org/10.3390/app13042570.

4. S. Attabi *et al.*, Mechanical and wear behaviors of 316L stainless steel after ball burnishing treatment, *Journal of Materials Research and Technology* **15** (2021) 3255, https://doi.org/10.1016/j.jmrt.2021.09.081.

5. A. Márquez-Herrera *et al.*, Calentador de sustratos compacto y de bajo costo para tratamiento térmico in situ de películas delgadas depositadas por rf-sputtering, *Rev. Mex. Fis.* **56** (2010) 85.

6. L. Lacalle *et al.*, The effect of ball burnishing on heat-treated steel and Inconel 718 milled surfaces, *The International Journal of Advanced Manufacturing Technology* **32** (2007) 958, https://doi.org/10.1007/s00170-005-0402-5.

7. A. Toloei, V. Stoilov, and D. Northwood, The effect of different surface topographies on the corrosion behaviour of nickel, *WIT Transactions on Engineering Science* **77** (2013) 193, https://doi.org/10.2495/MC130171.

8. L. Abosrra *et al.*, Corrosion of mild steel and 316L austenitic stainless steel with different surface roughness in sodium chloride saline solutions, *Corros.: Mater. Perf. Cathodic Prot.* (2009) 107, https://doi.org/10.2495/ECOR090161.

9. L. Jinlong, L. Hongyun, and L. tongxiang, Investigation of microstructure and corrosion behavior of burnished aluminum alloy by TEM, EWF, XPS and EIS techniques, *Materials Research Bulletin* **83** (2016) 148, https://doi.org/10.1016/j.materresbull.2016.05.013.

10. Z. D. Kadhim, M. A. Abdulrazzaq, and S. Q. AL-Shahrabalee, Burnishing Operation for Corrosion Resistance Improvement of AISI 1017 Carbon Steel, *European Journal of Engineering and Technology Research* **3** (2018) 21, https://doi.org/10.24018/ejeng.2018.3.6.749.

11. A. Saldaña-Robles *et al.*, Influence of ball-burnishing on roughness, hardness and corrosion resistance of AISI 1045 steel, *Surface and Coatings Technology* **339** (2018) 191, https://doi.org/10.1016/j.surfcoat.2018.02.013.

12. Z. Pu *et al.*, Grain refined and basal textured surface produced by burnishing for improved corrosion performance of AZ31B Mg alloy, *Corrosion Science* **57** (2012) 192, https://doi.org/10.1016/j.corsci.2011.12.018.

13. U. Al-Qawabeha, A. E. Al-Rawajfeh, and E. Al-Shamaileh, Influence of roller burnishing on surface properties and corrosion resistance in steel, *Anti-Corrosion Methods and Materials* **56** (2009) 261, https://dx.doi.org/10.1108/00035590910989552.

14. D. Silva-Álvarez *et al.*, Improving the surface integrity of the CoCrMo alloy by the ball burnishing technique, *Journal of Materials Research and Technology* **9** (2020) 7592, https://doi.org/10.1016/j.jmrt.2020.05.038.

15. S. Hiromoto, *Corrosion of metallic biomaterials*, pp. 131-152 (Elsevier, 2019), https://doi.org/10.1016/B978-0-08-102666-3.00004-3.

16. X. Sun, D. Sun, and L. Yang, Corrosion monitoring under cathodic protection conditions using multielectrode array sensors, *In Techniques for Corrosion Monitoring*, pp. 539-570 (Elsevier, 2021), https://doi.org/10.1016/B978-0-08-103003-5.00026-6.

17. T. M. Azeez *et al.*, Measurement of surface roughness on a transmission shaft using CNC and conventional lathes machining, *Int J Sci Technol* **8** (2019) 1626.

18. D. Ulutan and T. Ozel, Machining induced surface integrity in titanium and nickel alloys: A review, *International Journal of Machine Tools and Manufacture* **51** (2011) 250, https://doi.org/10.1016/j.ijmachtools.2010.11.003.

19. P. Zhang *et al.*, Effect of turning-induced initial roughness level on surface roughness and residual stress improvements in subsequent burnishing, *Archives of Civil and Mechanical Engineering* **20** (2020) 1, https://doi.org/10.1007/s43452-020-00083-5.

20. M. Solórzano *et al.*, Structural characterization, dielectric, and magnetic properties of Ti-doped YFeO 3 multiferroic compound, *Journal of Materials Science: Materials in Electronics* **31** (2020) 14478, https://doi.org/10.1007/s10854-020-04007-0.

21. N. X. ray Photoelectron Spectroscopy Database, NIST Standard Reference Database Number 20, *National Institute of Standards and Technology, Gaithersburg MD*, **20899** (2000), https://doi.org/10.18434/T4T88K.

22. X. Li *et al.*, Surface Integrity and Corrosion Performance of Biomedical Magnesium-Calcium Alloy Processed by Hybrid Dry Cutting-Finish Burnishing, *Journal of Materials Engineering and Performance* **30** (2021) 2462, https://doi.org/10.1007/s11665-021-05596-w.

23. X. Lazkano *et al.*, Roughness maps to determine the optimum process window parameters in face milling, *International Journal of Mechanical Sciences* **221** (2022) 107191, https://doi.org/10.1016/j.ijmecsci.2022.107191.

24. O. Zurita, V. Di-Graci, and M. Capace, Effect of cutting parameters on surface roughness in turning of annealed AISI-1020 steel, *Revista Facultad de Ingeniería* **27** (2018) 121, https://doi.org/10.19053/01211129.v27.n47.2018.7928.

25. B. S. Bokstein, M. I. Mendelev, and D. J. Srolovitz, Thermodynamics and kinetics in materials science: a short course (OUP Oxford, 2005).

26. A. A. García-Granada *et al.*, Ball-burnishing effect on deep residual stress on AISI 1038 and AA2017-T4, *Materials and Manufacturing Processes* **32** (2017) 1279, https://doi.org/10.1080/10426914.2017.1317351.

27. G. Wang *et al.*, Effect of residual stress and microstructure on corrosion resistance of carburised 18CrNiMo7-6 steel, *Anti-Corrosion Methods and Materials* **67** (2020) 357, https://doi.org/10.1108/ACMM-02-2020-2260.

28. A. Merkys *et al.*, COD:: CIF:: Parser: an error-correcting CIF parser for the Perl language, *Journal of applied crystallography* **49** (2016) 292, https://doi.org/10.1107/S1600576715022396.

29. Y.-J. Seo, Methodological Consideration on the Prediction of Electrochemical Mechanical Polishing Process Parameters by Monitoring of Electrochemical Characteristics of Copper Surface, *Journal of Electrochemical Science and Technology* **11** (2020) 346, https://doi.org/10.33961/jecst.2019.00640.

30. J. Jeong and H.-C. Shin, In-Depth Analysis of Coulombic Efficiency of Zinc-Air Secondary Batteries, *Journal of Electrochemical Science and Technology* **11** (2020) 26, https://doi.org/10.33961/jecst.2019.00339.

31. L. Jinlong and L. Hongyun, Effect of surface burnishing on texture and corrosion behavior of 2024 aluminum alloy, *Surface and Coatings Technology* **235** (2013) 513, https://dx.doi.org/10.1016/j.surfcoat.2013.07.071.